

Geometric frustration of Jahn–Teller order in the infinite-layer lattice

<https://doi.org/10.1038/s41586-022-05681-2>

Received: 5 April 2022

Accepted: 22 December 2022

Published online: 22 February 2023

 Check for updates

Woo Jin Kim^{1,2}, Michelle A. Smeaton³, Chunjing Jia^{1,4}, Berit H. Goodge^{5,6}, Byeong-Gwan Cho⁷, Kyuho Lee^{1,8}, Motoki Osada^{1,9}, Daniel Jost¹, Anton V. Levlev¹⁰, Brian Moritz¹, Lena F. Kourkoutis^{5,6}, Thomas P. Devereaux^{1,9} & Harold Y. Hwang^{1,2}

The Jahn–Teller effect, in which electronic configurations with energetically degenerate orbitals induce lattice distortions to lift this degeneracy, has a key role in many symmetry-lowering crystal deformations¹. Lattices of Jahn–Teller ions can induce a cooperative distortion, as exemplified by LaMnO₃ (refs. ^{2,3}). Although many examples occur in octahedrally⁴ or tetrahedrally⁵ coordinated transition metal oxides due to their high orbital degeneracy, this effect has yet to be manifested for square-planar anion coordination, as found in infinite-layer copper^{6,7}, nickel^{8,9}, iron^{10,11} and manganese oxides¹². Here we synthesize single-crystal CaCoO₂ thin films by topotactic reduction of the brownmillerite CaCoO_{2.5} phase. We observe a markedly distorted infinite-layer structure, with ångström-scale displacements of the cations from their high-symmetry positions. This can be understood to originate from the Jahn–Teller degeneracy of the d_{xz} and d_{yz} orbitals in the d⁷ electronic configuration along with substantial ligand–transition metal mixing. A complex pattern of distortions arises in a $2\sqrt{2} \times 2\sqrt{2} \times 1$ tetragonal supercell, reflecting the competition between an ordered Jahn–Teller effect on the CoO₂ sublattice and the geometric frustration of the associated displacements of the Ca sublattice, which are strongly coupled in the absence of apical oxygen. As a result of this competition, the CaCoO₂ structure forms an extended two-in–two-out type of Co distortion following ‘ice rules’¹³.

The cooperative Jahn–Teller effect (JTE) often induces strong coupling between charge, orbital and magnetic ordering, which has been related to many correlated phenomena such as colossal magnetoresistance^{14,15} and superconductivity¹⁶. For the magnetoresistance associated with the metal–insulator transition in perovskite-based manganites, it has been established that the double-exchange model for magnetism cannot solely account for the large resistivity drop below the paramagnetic-to-ferromagnetic phase transition, and rather that a strong electron–phonon interaction arising from the JTE plays a crucial role^{17–20}. Moreover, single-layered perovskite (La,A)₂CuO₄ (where A is Sr or Ba) shows unconventional superconductivity within Jahn–Teller (JT)-distorted CuO₆ octahedra, indicating the important role of the JTE in many correlated ground states²¹.

Despite its generality, the study of the cooperative JTE in oxides has been largely confined to octahedral and tetrahedral coordination. In perovskites, octahedral-site cations having outer-electron configurations of d⁴, d⁷ or d⁹ (ref. ⁴) are often JT-active systems, splitting the partially filled e_g orbitals (Fig. 1a). In LaMnO₃ with high-spin state d⁴, the partially filled e_g orbitals of Mn³⁺ induces both MnO₆ octahedral distortion (that is, the Q₃JT distortion)¹ and d_{z2}-orbital ordering to reduce its total energy (Fig. 1b), resulting in an orthorhombic crystal structure (Fig. 1c). The cooperative JTE has also been observed in spinel structures with tetrahedral-site

cations having d⁴ or d⁹ configurations⁵. The JTE in a square-planar anion configuration has been theoretically discussed from the foundations of the concept: that a Q₂ vibrational mode will distort the high-symmetry square coordination to a low-symmetry rhombus¹. The FeO₄ chromophore molecule exhibits nearly square-planar coordination, which is thought to be JT driven from the expected tetrahedral structure²². However, a pure cooperative Q₂JT distortion has not been experimentally observed in crystalline materials hosting square-planar-coordinated cations.

The infinite-layer structure provides a unique platform to explore this possibility and the potential cooperative response in a lattice of JT ions. This structure forms a four-coordinated transition metal oxide with a two-dimensional (2D) square lattice, which can often be derived from precursor higher oxides by de-intercalating the apical oxygen using topotactic reduction (Fig. 2a). These 2D oxides were first synthesized in powder nickelates with an extremely low nickel valence state (Ni⁺¹) (ref. ⁸). The same four-coordinated system has also been found in copper oxide superconductors^{6,7}. Subsequently, the iron oxide infinite-layer structure was discovered with antiferromagnetic ground states^{10,11}. In addition, recently, hole-doped infinite-layer nickelates with Ni 3d^{9–6} have been found to be superconducting^{23,24}.

Within this quasi-2D structure, how the orbital degeneracy affects the crystal and electronic structure is an open experimental question.

¹Stanford Institute for Materials and Energy Sciences, SLAC National Accelerator Laboratory, Menlo Park, CA, USA. ²Department of Applied Physics, Stanford University, Stanford, CA, USA.

³Department of Materials Science and Engineering, Cornell University, Ithaca, NY, USA. ⁴Department of Physics, University of Florida, Gainesville, FL, USA. ⁵School of Applied and Engineering Physics, Cornell University, Ithaca, NY, USA. ⁶Kavli Institute at Cornell for Nanoscale Science, Cornell University, Ithaca, NY, USA. ⁷Pohang Accelerator Laboratory, POSTECH, Pohang, Republic of Korea. ⁸Department of Physics, Stanford University, Stanford, CA, USA. ⁹Department of Materials Science and Engineering, Stanford University, Stanford, CA, USA. ¹⁰Center for Nanophase Materials Sciences Oak Ridge National Laboratory, Oak Ridge, TN, USA. [✉]e-mail: wjk316@stanford.edu; hyhwang@stanford.edu

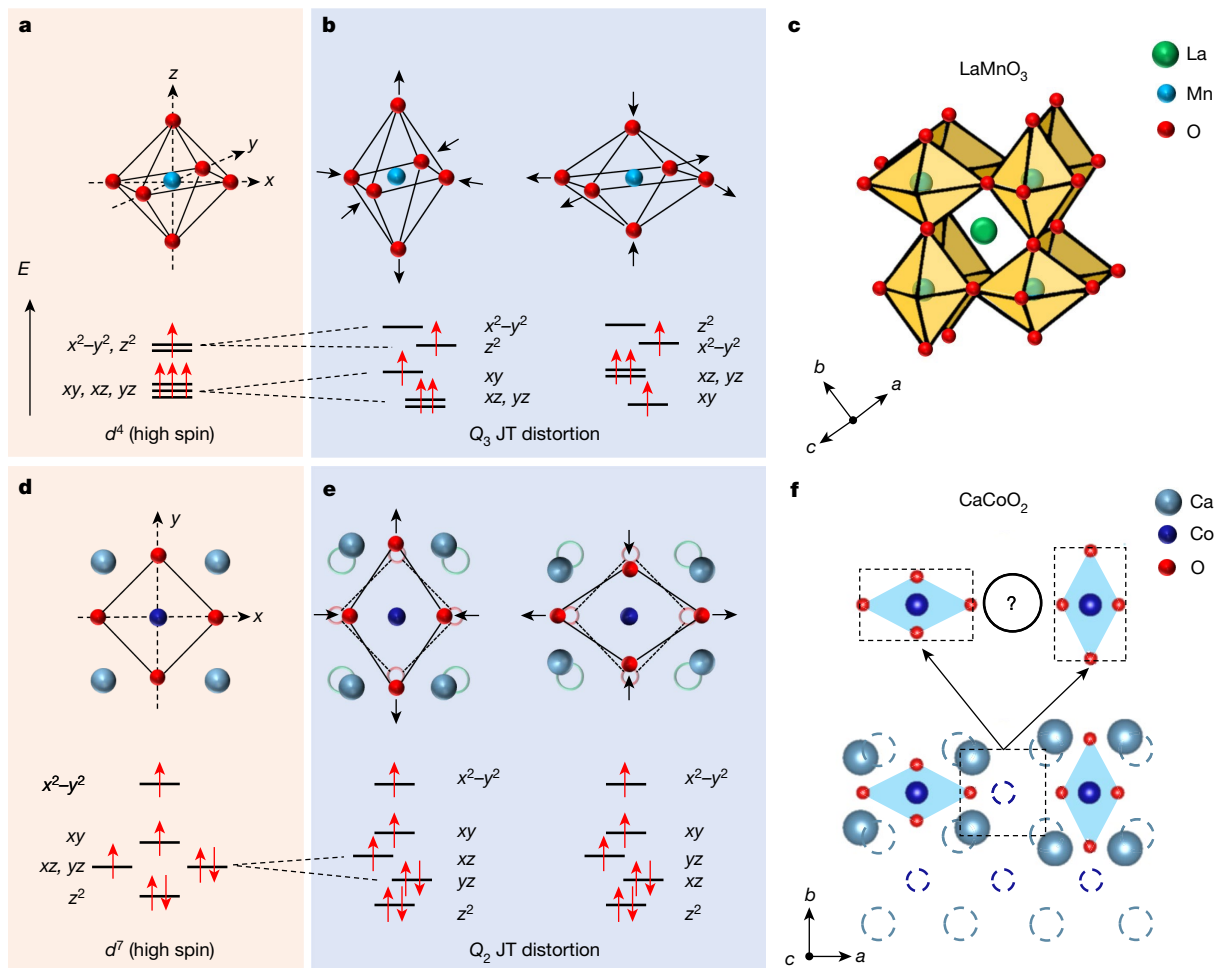


Fig. 1 | JT distortion in 3D and 2D oxide lattices. **a**, Schematic MO_6 (where M is a transition metal) octahedron and crystal field structure for a high-spin d^4 electron configuration. **b**, Octahedral distortions and associated orbital levels for a Q_3 JT distortion. **c**, Strong Q_3 JT-distorted LaMnO_3 crystal structure with high-spin $d^4 \text{Mn}^{3+}$ as an example of a cooperative JT distortion. **d**, Schematic

square-planar MO_4 plaquette and crystal field structure for a high-spin d^7 electron configuration. **e**, Square-planar distortion and associated orbital levels for a Q_2 JT distortion. **f**, Displacements in the Ca layer in CaCoO_2 , arising from strong interlayer coupling in the absence of apical oxygen, geometrically frustrate a simple cooperative JT distortion analogous to LaMnO_3 .

The crystal field structure for the square-planar coordination is quite different from that of octahedral or tetrahedral coordination, with lower overall degeneracy. As shown in Fig. 1d, only the d_{xz} and d_{yz} orbitals are degenerate. Therefore, to be JT active, the system should have a partially filled d_{xz} (or d_{yz}) orbital state. The high-spin d^7 configuration meets these conditions, making the infinite-layer cobaltates (stabilized here in CaCoO_2) with Co^{2+} oxidation state an ideal candidate. Considering only the CoO_2 plane, one might expect a cooperative JTE to induce an orbitally ordered lattice of d_{xz} or d_{yz} orbital states in analogy to LaMnO_3 (Fig. 1e). However, the absence of apical oxygen gives rise to strong electrostatic coupling between the CoO_2 and Ca layers—an interaction that is largely screened for octahedral coordination. As we will show, this interlayer coupling gives rise to a geometric frustration of the induced Ca displacements (Fig. 1f), which is in competition with the cooperative JTE.

Ångström-scale cation displacements in CaCoO_2

Here we stabilized an infinite-layer compound CaCoO_2 with dramatic in-plane lattice distortions. The starting point is the synthesis of epitaxial single-crystal thin films of brownmillerite $\text{CaCoO}_{2.5}$ on strontium titanum oxide (SrTiO_3) (001) substrates (Methods; θ -diffraction angle (2θ) symmetric X-ray diffraction (XRD) scan in Fig. 2b)²⁵. The high-angle annular dark-field (HAADF) scanning transmission electron microscopy

(STEM) image of $\text{CaCoO}_{2.5}$ (Extended Data Fig. 1a) confirms the excellent crystallinity with abrupt interfaces with the substrate and subsequent SrTiO_3 capping layer, which is used to stabilize the reduced phase. The $\text{CaCoO}_{2.5}$ heterostructure was then reduced using calcium hydride (CaH_2), after which the XRD symmetric scan shows only peaks corresponding to the infinite-layer structure (00l) (Fig. 2c), with a substantial contraction of the out-of-plane lattice parameter (c_t) from about 3.72 Å to about 3.27 Å. From reciprocal space mapping, we extract the in-plane lattice constant (a_t) of CaCoO_2 to be about 3.86 Å (Extended Data Fig. 1b), indicating that the reduced film is relaxed from the substrate.

The large c -axis difference between CaCoO_2 and CaCoO_3 (ref. ²⁶) closely follows trends of known infinite-layer oxides (Extended Data Fig. 1c). Furthermore, electron energy loss spectroscopy (EELS) of the $\text{CaCoO}_{2.5}$ and CaCoO_2 films (Extended Data Fig. 2) is consistent with a transition from Co^{3+} to Co^{2+} (ref. ²⁷). It is noted that SrCoO_2 has been previously synthesized by reduction from $\text{SrCoO}_{2.5}$ (ref. ²⁸). However, SrCoO_2 has a much larger c_t (about 3.76 Å) with tetrahedrally coordinated Co^{2+} —that is, a fundamentally different structure²⁸. Moreover, chemical characterization by time-of-flight secondary-ion mass spectrometry (TOF-SIMS) shows no sign of hydrogen intercalation in CaCoO_2 (Extended Data Fig. 3a), unlike structures such as SrCoO_xH_y (refs. ^{29,30}). To our knowledge, the infinite-layer structure we observe has not previously been reported for cobalt oxides.

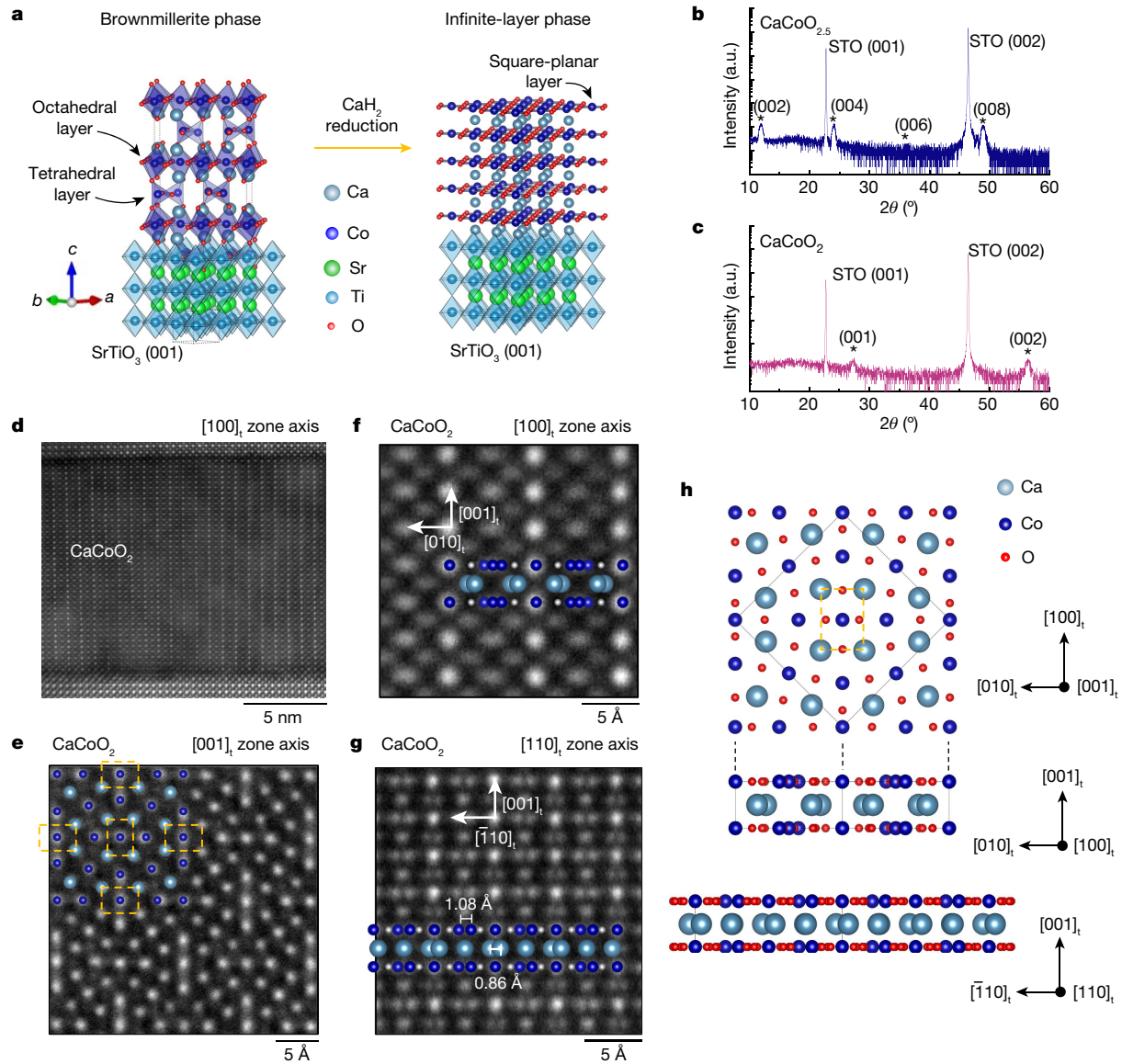


Fig. 2 | Synthesis and large-scale cation displacements in thin-film CaCoO_2 . **a**, Schematic of the topotactic reduction of brownmillerite $\text{CaCoO}_{2.5}$ (left) to infinite-layer CaCoO_2 (right). **b,c**, XRD θ - 2θ symmetric scans of 18-nm-thick $\text{CaCoO}_{2.5}$ (**b**) and CaCoO_2 (**c**) films capped with 2-nm-thick SrTiO_3 (STO) layers grown on SrTiO_3 (001) substrates. Asterisks indicate the diffraction peaks of the thin films. **d**, HAADF-STEM image of the $[100]_t$ zone axis of CaCoO_2 . **e**, Plan-view HAADF-STEM image of CaCoO_2 . The distorted Ca layer is clearly seen in

the image (yellow dashed rectangles). **f,g**, High-magnification HAADF-STEM images of CaCoO_2 along the $[100]_t$ (**f**) and $[110]_t$ (**g**) zone axes. Dark (bright) blue balls indicate Co (Ca) cations and grey balls indicate oxygen. The atomic positions of oxygen here are shown for the ideal square-planar sites. **h**, Cation unit-cell structure of CaCoO_2 based on HAADF-STEM. The red solid balls indicate the oxygen positions after GIXRD refinement.

The HAADF-STEM image along the SrTiO_3 $[100]$ zone axis (Fig. 2d) shows that CaCoO_2 has a very strong in-plane superlattice modulation, unlike all known infinite-layer systems^{6,9,10,31}. A closer look at the CaCoO_2 layer along the $[100]_t$ zone axis in Fig. 2f shows that this is due to in-plane cation displacements from the simple tetragonal infinite-layer structure. These are more clearly visible along the $[110]_t$ zone axis (Fig. 2g), which reveals that both Co and Ca ions have alternating sites with very large splitting of 1.08 Å and 0.86 Å, respectively. Beyond these substantial in-plane distortions, there are no observable accompanying out-of-plane atomic distortions (Extended Data Fig. 3b–d). The θ - 2θ asymmetric XRD scan also rules out a possible c -lattice doubling (Extended Data Fig. 4). The plan-view HAADF-STEM image in Fig. 3e also shows strong in-plane superlattice modulation. In aggregate, these results show that the cation lattice is described by a tetragonal supercell $2\sqrt{2}a_t \times 2\sqrt{2}a_t \times c_t$ ($a = b = 2\sqrt{2}a_t = 10.78$ Å and $c = c_t = 3.27$ Å) in the

P42₁2 symmetry group as shown in Fig. 2h (see Extended Data Table 1 for atomic coordinates). The projections of this crystal structure are shown in Fig. 2e–g, in close correspondence with the STEM images.

Structural refinement of the oxygen positions in CaCoO_2

Given the extremely small sample volume and low relative X-ray and electron scattering cross-sections for oxygen, determining their positions is quite challenging. Nevertheless, we can refine the oxygen positions from high-resolution synchrotron grazing incidence XRD (GIXRD) of the in-plane superlattice diffraction peaks (Fig. 3a). Using the cation coordinates from STEM, we first simulated the XRD pattern to find the seven strongest in-plane superlattice peaks (Extended Data Table 2) assuming undistorted oxygen positions. These were then used to experimentally

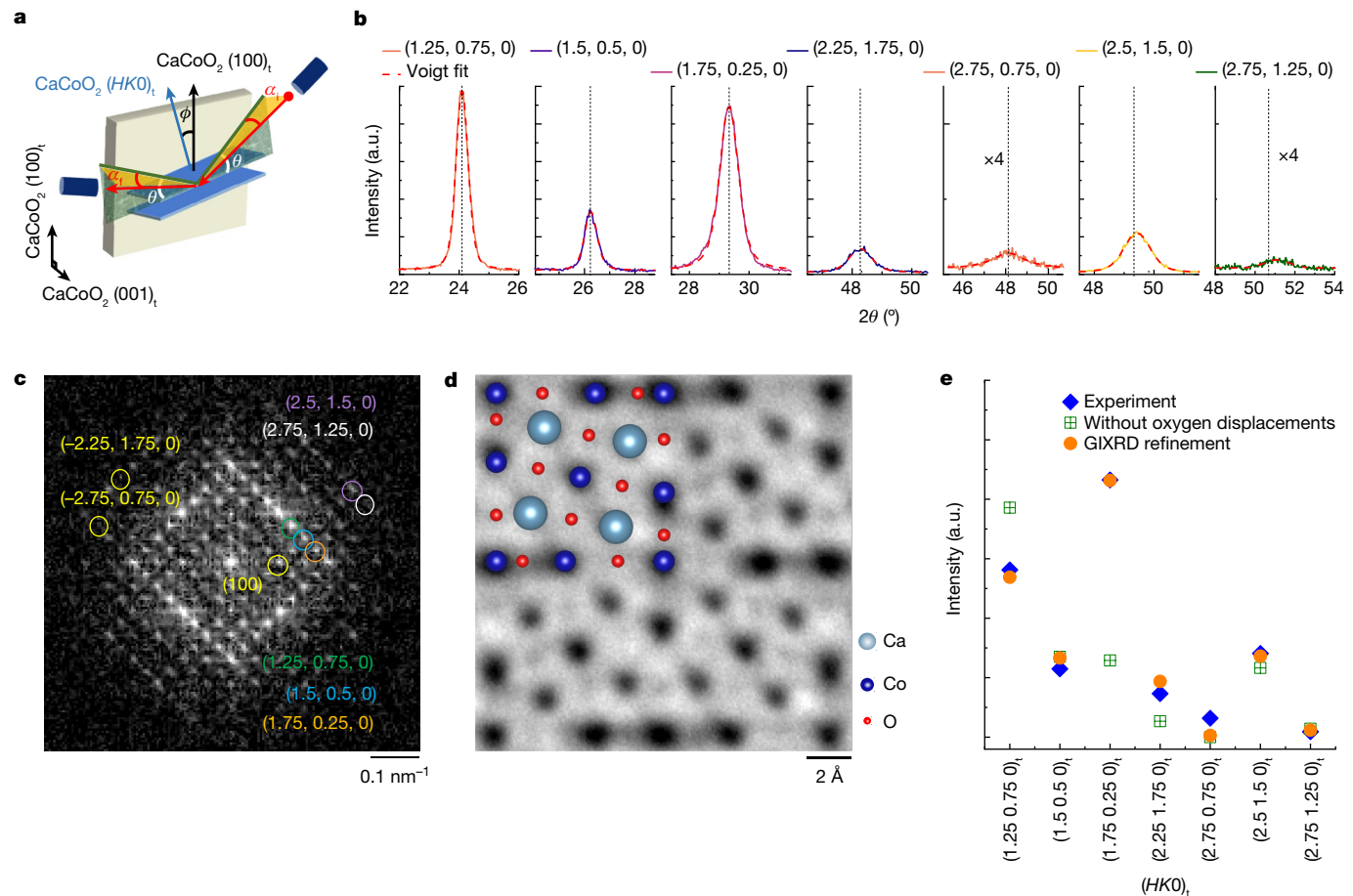


Fig. 3 | GIXRD and refinement of the oxygen positions. **a**, Schematic of the GIXRD experimental geometry. α_i and α_r are the incident and reflected angle, respectively, which are maintained to be 0.2° for all measurements. ϕ is the angle between $\text{CaCoO}_2(100)_t$ and $(HKO)_t$, and θ is the diffraction angle for $\text{CaCoO}_2(HKO)_t$ planes. **b**, GIXRD θ - 2θ scans for various $\text{CaCoO}_2(HKO)_t$ planes. The red dashed lines indicate Voigt fitting results. **c**, Fast Fourier transform of a plan-view HAADF-STEM image. All seven GIXRD peaks are observed. **d**, Unit-cell-

averaged plan-view ABF-STEM image of CaCoO_2 with the final refined structure model overlayed. Dark contrast indicates the atomic columns. **e**, Relative integrated intensity for all $\text{CaCoO}_2(HKO)_t$ GIXRD peaks. The blue (orange) filled diamonds (circles) are experimental (GIXRD refinement) results. The green crossed squares are calculated GIXRD intensity for CaCoO_2 in the absence of oxygen displacements (oxygen positions for an ideal square plane).

search for the actual scattering peaks, all of which were found very close to the simulated positions (Fig. 3b and Extended Data Table 2), confirming the overall structural symmetry deduced from the STEM results. The fast Fourier transform of the plan-view HAADF-STEM image in Fig. 2e also confirms the existence of the seven in-plane peaks observed from the GIXRD measurements (Fig. 3c). The approximate oxygen positions can also be extracted via plan-view annular bright-field (ABF)-STEM imaging (Fig. 3d). These were taken as the starting positions for Rietveld refinement of the relative intensities of the GIXRD peaks (blue diamonds in Fig. 3e; see Methods and Extended Data Tables 1 and 3). The refinement was dominated by oxygen displacements, such that the initial R factor of about 0.46 with undistorted oxygen (green squares in Fig. 3e) reduced to about 0.08 (orange circles in Fig. 3e), indicative of a high-quality fit. The overlay of the final refined structure of CaCoO_2 in Fig. 3d shows a good qualitative match with the experimental results within the precision of the ABF-STEM measurement.

Origin of the ordered distortions in CaCoO_2

Figure 4a highlights the three distinct CoO_4 plaquettes (for $\text{Co}_{(1)}$, $\text{Co}_{(2)}$ and $\text{Co}_{(3)}$, coordinated by three distinct oxygen sites) in blue, green and orange, respectively, for the refined structure of CaCoO_2 . The blue $\text{Co}_{(1)}\text{O}_4$ plaquette shows strong JT distortion as predicted¹: the bonding length

between $\text{Co}_{(1)}$ and $\text{O}_{(2)}$ ($d_{\text{Co}_{(1)}-\text{O}_{(2)}}$) is $2.09 \pm 0.01 \text{ \AA}$ whereas that between $\text{Co}_{(1)}$ and $\text{O}_{(3)}$ ($d_{\text{Co}_{(1)}-\text{O}_{(3)}}$) is $1.19 \pm 0.01 \text{ \AA}$. It is noted that the anisotropic bonding ratio $d_{\text{Co}_{(1)}-\text{O}_{(2)}}/d_{\text{Co}_{(1)}-\text{O}_{(3)}}$ (1.76 ± 0.02) is extraordinarily large, for example, compared with the value for the JT-distorted octahedra in LaMnO_3 (about 1.15)². The green $\text{Co}_{(2)}\text{O}_4$ plaquette is trapezoidal with three different Co–O bonding lengths, whereas that for $\text{Co}_{(3)}$ (orange) maintains four-fold symmetry (with rotation). Surprisingly, only 25% of the Co is strongly JT distorted, in contrast to the cooperative JTE in LaMnO_3 that provides an equivalent JT octahedral distortion for every Mn site (Fig. 1c).

This intriguing situation can be understood to originate from the competition between the JT distortion and an induced geometrical frustration in the Ca layer. As shown by the dashed rectangles in Fig. 4a, the strong JTE distorts not only the $\text{Co}_{(1)}\text{O}_4$ but also the Ca layer. This unusual coupling of Ca to the Q_2 JT distortion arises from the lack of apical oxygen, which gives rise to strong electrostatic coupling between the CoO_2 and Ca layers. The anisotropic distortions of the Ca layer are however highly geometrically frustrated between neighbouring sites (Fig. 1f). Consequently, a complex arrangement of displacements is observed.

Interestingly, the geometrical frustration of the cooperative JTE results in a two-in-two-out type of distortion pattern, following ‘ice rules’¹³ for the ångström-scale displacements of $\text{Co}_{(2)}$ around the maximally JT-distorted $\text{Co}_{(1)}\text{O}_4$ (Fig. 4a). The $\text{Co}_{(2)}\text{O}_4$ plaquette notably breaks

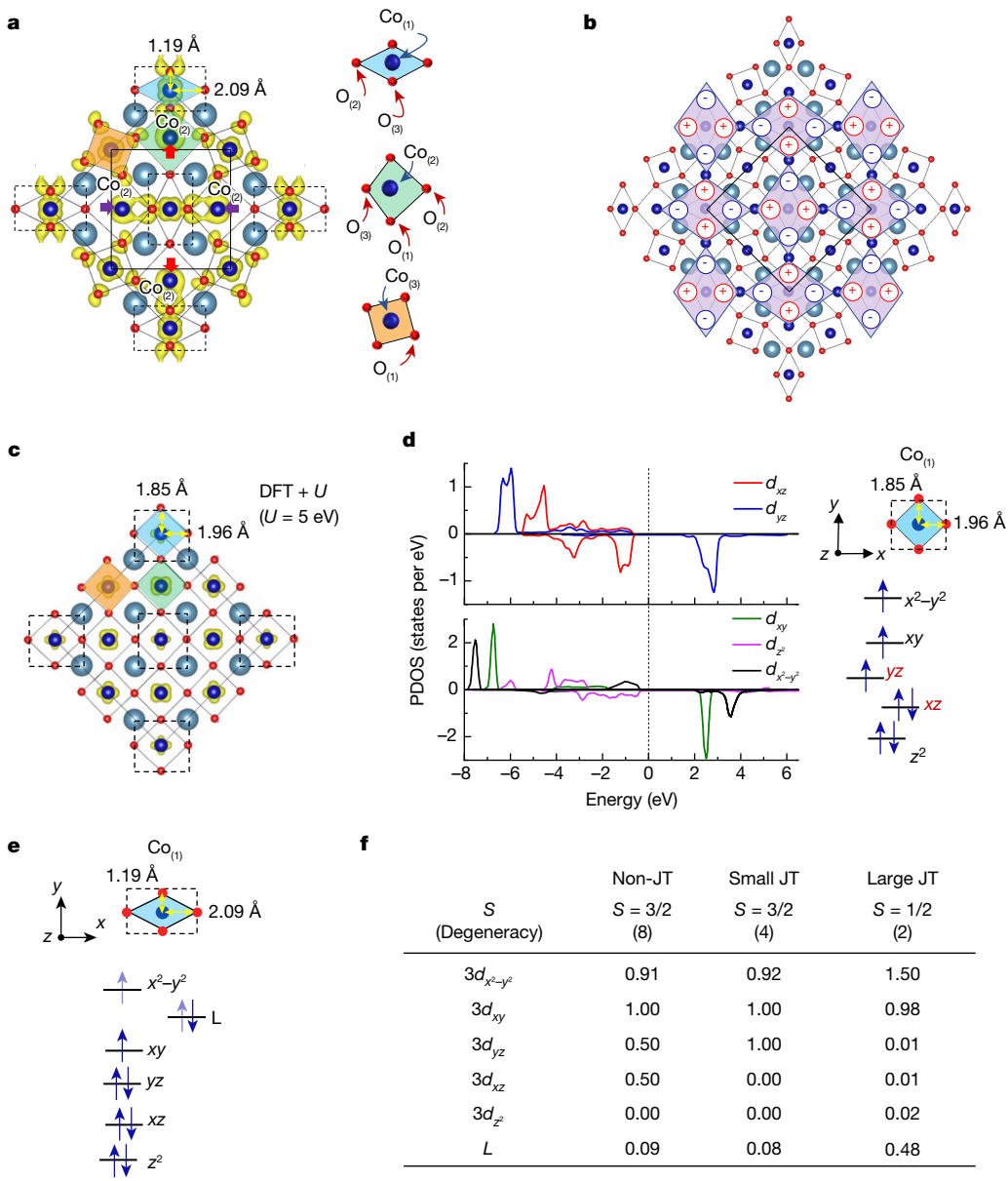


Fig. 4 | Extended structure of CaCoO_2 , ice rules, quadrupolar ordering and electronic structure. **a**, Plan view of the experimentally refined crystal structure of CaCoO_2 , consisting of three different CoO_4 sites corresponding to the three different colours (blue, green and orange). The blue-coloured CoO_4 plaquettes are strongly JT distorted. In the full unit cell, a pair of $\text{Co}_{(2)}$ ions distort towards (purple arrows) the central $\text{Co}_{(1)}$, whereas the other pair of $\text{Co}_{(2)}$ ions distort outwards (red arrows) from the central $\text{Co}_{(1)}$. The visualized isosurface in yellow colour represents the electron density for the lowest unoccupied $d_{x^2-y^2}$ band for $\text{Co}_{(1)}$ at the gamma point. **b**, The dipole arrangements associated with $\text{Co}_{(2)}$ displacements form an ordered array of electric quadrupoles (purple diamonds). **c**, Plan view of the computationally relaxed crystal structure of CaCoO_2 from DFT + U ($U = 5$ eV) calculations. This consists of three different

CoO_4 sites, which show the same structural symmetry as experiment, but with much smaller distortions. The visualized isosurface in yellow colour represents the electron density for the lowest unoccupied $d_{x^2-y^2}$ band for $\text{Co}_{(1)}$ at the gamma point. **d**, The spin-dependent PDOS of $\text{Co}_{(1)}$ d orbitals from DFT + U and the corresponding atomic energy level diagram for the relaxed structure. **e**, An atomic energy level diagram appropriate for the experimentally refined structure from a ligand–multiplet calculation. The light blue arrows represent the occupation of half an electron. **f**, A table showing the number of holes from ligand–multiplet calculations. The three columns give results in the absence of distortions (non-JT), for parameters appropriate for the DFT + U relaxed structure (small JT) and for parameters appropriate for the experimentally refined structure (large JT).

inversion symmetry, and thus the long-range-ordered structure can be viewed as an ordering of electric dipoles. From an electrostatic point of view, this is equivalent to a ‘herringbone’ arrangement of electric quadrupoles (Fig. 4b), which minimizes the electrostatic interaction between quadrupole moments³².

To further understand CaCoO_2 , we performed density functional theory (DFT) + on-site Coulomb interaction (U) calculations. The overall symmetry for the relaxed structure directly matches the experimental observations, and it is robust to variations in U (Extended Data Fig. 5a).

However, the magnitude of the distortions is substantially smaller—for example, the calculated anisotropic bonding ratio of about 1.06 is much less than the experimentally observed ratio of 1.76 ± 0.02 . The electronic band structure of CaCoO_2 shows an insulating ground state with a bandgap energy of $E_g \approx 0.670$ eV (Extended Data Fig. 5b). Experimentally, the resistivity exhibits insulating temperature dependence (Extended Data Fig. 5c).

The spin-dependent partial density of states (PDOS) for $\text{Co}_{(1)}$ shows that the d_{z^2} and d_{xz} orbitals are doubly occupied (Fig. 4d) as expected

Article

from strong JT splitting in a square-planar geometry (absence of apical ligands), and the d_{yz} orbital opens a gap between occupied and unoccupied states as indicated earlier (Fig. 1e). Overall, $\text{Co}_{(1)}$ is in a d^7 configuration where a spin-down hole resides in both the $d_{x^2-y^2}$ and d_{xy} orbitals, with an additional spin-down hole in d_{yz} orbitals (Figs. 1d and 4d). In contrast, the spin-dependent PDOS for $\text{Co}_{(3)}$ sites show degenerate d_{xz} and d_{yz} orbitals owing to the square symmetry of $\text{Co}_{(3)}\text{O}_4$ (Extended Data Fig. 5d,e). These results are consistent with expectations from the simple crystal field structure in Fig. 1e, indicating that the JTE, together with electron correlations, drives the symmetry lowering distortion and lifts the orbital degeneracy.

We further compared the total energy of the non-JT-distorted structure, a $\sqrt{2} \times \sqrt{2} \times 1$ supercell with a purely Q_2 JT distortion, and the relaxed structure to see whether the structure can be stabilized solely by Q_2 JT distortions. Interestingly, the result shows that $\sqrt{2} \times \sqrt{2} \times 1$ supercell with purely Q_2 JT distortion is energetically more stable than a square-planar lattice without any distortion (Extended Data Fig. 6a). However, our DFT calculations with various starting points show that the structure always converged to the current DFT-relaxed structure, confirming that this structure minimizes the total energy (Extended Data Fig. 6b,c).

The quantitative discrepancy in the scale of distortions between experiment and theory may indicate the presence of large molecular orbital effects in this system that are difficult to capture using one-electron approaches^{33,34}. Unlike octahedrally coordinated d^4 systems, the Q_2 JT distortion, which splits the d_{xz} and d_{yz} orbitals, draws the ligands along one direction inwards, towards $\text{Co}_{(1)}$. This substantially increases the hybridization of the σ -bonded $\text{Co}_{(1)}-\text{O}$ orbitals (Fig. 4a), encouraging a strong admixture of holes on the neighbouring oxygen. Evidence for this tendency can be seen in the electron density distribution computed using the experimentally refined atomic positions (yellow isosurface in Fig. 4a), which is much more extended with substantial weight on oxygen when compared with the computationally relaxed structure (yellow isosurface in Fig. 4c). Thus a ‘negative charge transfer’ material may result, with trimerized molecular orbitals of $\text{Co}(3d_{x^2-y^2})-\text{O}(2p_x)$ hybrids, transitioning from high-spin Co $3d^7$ to a low-spin state $\text{Co}3d^8\text{L}$, where L denotes a ligand hole dispersed among the neighbouring σ -bonded oxygens (Fig. 4e). In fact, this could be the driving force behind the observed quadrupolar ordering (Fig. 4b).

Performing a small cluster exact diagonalization calculation for an 11-orbital unit cell (5 Co $3d$ and 3 O $2p_{xy}$ orbitals; see Methods; result shown in Fig. 4f) confirms this picture. While a small JT splitting gives the DFT-relaxed configuration (high-spin $3d^7$), increasing the hybridization between Co and O along one direction, as in the experimental structure, draws electron weight from O $2p_y$ to Co $3d_{x^2-y^2}$ (Fig. 4f), raising the $3d_{x^2-y^2}$ complex above the $3d_{xy/xz}$ orbitals, further reducing the degeneracy. This low-spin $3d^8\text{L}$ configuration is common to other Co-based negative-charge-transfer systems such as $\text{SrCoO}_{2.5}$ (ref. ³⁵) and SrCoO_3 (ref. ³⁶). Its presence in this system is further supported by O K-edge EELS (Extended Data Fig. 2d), which shows a pre-peak in good agreement with the hybridization pre-peak observed in $\text{SrCoO}_{3-\delta}$ ($\delta \leq 0.5$)³⁷.

Conclusion

In summary, we have found CaCoO_2 to be a model system for realizing the 2D JT lattice with square-planar coordination. In contrast to layered perovskite-based systems with equivalent octahedral distortions^{38–40}, the interlayer coupling between the Ca layer and the CoO_2 layer is strong, such that the distorted structure is governed by the underlying competition between the JTE and the geometric frustration induced in the Ca layer. This leads to a complex pattern of distortions that arise in a $2\sqrt{2}a_t \times 2\sqrt{2}a_t \times c_t$ unit cell and substantial ligand-transition metal mixing. The understanding of the JTE

here may have general implications for complex compounds with 2D atomic layers where both interlayer coupling and the JTE are prominent.

Online content

Any methods, additional references, Nature Portfolio reporting summaries, source data, extended data, supplementary information, acknowledgements, peer review information; details of author contributions and competing interests; and statements of data and code availability are available at <https://doi.org/10.1038/s41586-022-05681-2>.

1. Jahn, H. A. & Teller, E. Stability of polyatomic molecules in degenerate electronic states I—orbital degeneracy. *Proc. R. Soc. Lond.* **161**, 220–235 (1937).
2. Goodenough, J. B. Theory of the role of covalence in the perovskite-type manganites [$\text{La}_x\text{M}(\text{II})\text{MnO}_3$]. *Phys. Rev.* **100**, 564–573 (1955).
3. Gehring, G. A. & Gehring, K. A. Co-operative Jahn-Teller effects. *Rep. Prog. Phys.* **38**, 1–89 (1975).
4. Goodenough, J. B. Jahn-Teller phenomena in solids. *Annu. Rev. Mater. Sci.* **28**, 1–27 (1998).
5. Goodenough, J. B. Jahn-Teller distortions induced by tetrahedral-site Fe^{2+} ions. *J. Phys. Chem. Solids* **25**, 151–160 (1964).
6. Siegrist, T., Zahirak, S. M., Murphy, D. W. & Roth, R. S. The parent structure of the layered high-temperature superconductors. *Nature* **334**, 231–232 (1988).
7. Smith, M. G., Manthiram, A., Zhou, J., Goodenough, J. B. & Markert, J. T. Electron-doped superconductivity at 40 K in the infinite-layer compound $\text{Sr}_{1-y}\text{Nd}_y\text{CuO}_2$. *Nature* **351**, 549–551 (1991).
8. Crespin, M., Levitz, P. & Gatineau, L. Reduced forms of LaNiO_3 perovskite. Part 1—Evidence for new phases: $\text{La}_2\text{Ni}_2\text{O}_5$ and LaNiO_2 . *J. Chem. Soc. Faraday Trans. 2* **79**, 1181–1194 (1983).
9. Hayward, M. A., Green, M. A., Rosseinsky, M. J. & Sloan, J. Sodium hydride as a powerful reducing agent for topotactic oxide deintercalation: synthesis and characterization of the nickel(I) oxide LaNiO_2 . *J. Am. Chem. Soc.* **121**, 8843–8854 (1999).
10. Tsujimoto, Y. et al. Infinite-layer iron oxide with a square-planar coordination. *Nature* **450**, 1062–1065 (2007).
11. Kawakami, T. et al. Spin transition in a four-coordinate iron oxide. *Nat. Chem.* **1**, 371–376 (2009).
12. Dixon, E., Hadermann, J., Ramos, S., Goodwin, A. L. & Hayward, M. A. Mn(I) in an extended oxide: the synthesis and characterization of $\text{La}_{1-x}\text{Ca}_x\text{MnO}_{2+\delta}$ ($0.6 \leq x \leq 1$). *J. Am. Chem. Soc.* **133**, 18397–18405 (2011).
13. Pauling, L. The structure and entropy of ice and of other crystals with some randomness of atomic arrangement. *J. Am. Chem. Soc.* **57**, 2680–2684 (1935).
14. von Helmolt, R., Wecker, J., Holzapfel, B., Schultz, L. & Samwer, K. Giant negative magnetoresistance in perovskitelike $\text{La}_{2/3}\text{Ba}_{1/3}\text{MnO}_x$ ferromagnetic films. *Phys. Rev. Lett.* **71**, 2331–2333 (1993).
15. Raveau, B., Hervieu, M., Maignan, A. & Martin, C. The route to CMR manganites: what about charge ordering and phase separation? *J. Mater. Chem.* **11**, 29–36 (2001).
16. Han, J. E., Gunnarsson, O. & Crespi, V. H. Strong superconductivity with local Jahn-Teller phonons in Ce_60 solids. *Phys. Rev. Lett.* **90**, 167006 (2003).
17. Millis, A. J., Littlewood, P. B. & Shraiman, B. I. Double exchange alone does not explain the resistivity of $\text{La}_{1-x}\text{Sr}_x\text{MnO}_3$. *Phys. Rev. Lett.* **74**, 5144–5147 (1995).
18. Millis, A. J., Shraiman, B. I. & Mueller, R. Dynamic Jahn-Teller effect and colossal magnetoresistance in $\text{La}_{1-x}\text{Sr}_x\text{MnO}_3$. *Phys. Rev. Lett.* **77**, 175–178 (1996).
19. Röder, H., Zang, J. & Bishop, A. R. Lattice effects in the colossal-magnetoresistance manganites. *Phys. Rev. Lett.* **76**, 1356–1359 (1996).
20. Guzmán-Verri, G. G., Brieler, R. T. & Littlewood, P. B. Cooperative elastic fluctuations provide tuning of the metal-insulator transition. *Nature* **576**, 429–432 (2019).
21. Keller, H., Bussmann-Holder, A. & Müller, K. A. Jahn-Teller physics and high- T_c superconductivity. *Mater. Today* **11**, 38–46 (2008).
22. Wurzenberger, X., Piotrowski, H. & Klüfers, P. A stable molecular entity derived from rare iron(II) minerals: the square-planar high-spin- d^6 $\text{Fe}_{1/2}\text{O}_4$ chromophore. *Angew. Chem. Int. Ed.* **50**, 4974–4978 (2011).
23. Li, D. et al. Superconductivity in an infinite-layer nickelate. *Nature* **572**, 624–627 (2019).
24. Zeng, S. et al. Phase diagram and superconducting dome of infinite-layer $\text{Nd}_{1-x}\text{Sr}_x\text{NiO}_2$ thin films. *Phys. Rev. Lett.* **125**, 147003 (2020).
25. Boullay, P. et al. Structure determination of a brownmillerite $\text{Ca}_2\text{Co}_2\text{O}_5$ thin film by precession electron diffraction. *Phys. Rev. B* **79**, 184108 (2009).
26. Xiang, L. et al. Exceptional oxygen evolution reactivities on CaCoO_3 and SrCoO_3 . *Sci. Adv.* **5**, eaav6262 (2022).
27. Wang, Z. L. & Yin, J. S. Cobalt valence and crystal structure of $\text{La}_{0.5}\text{Sr}_{0.5}\text{CoO}_{2.25}$. *Phil. Mag. B* **77**, 49–65 (1998).
28. Li, H.-B. et al. Dehydration of electrochemically protonated oxide: SrCoO_2 with square spin tubes. *J. Am. Chem. Soc.* **143**, 17517–17525 (2021).
29. Hayward, M. A. et al. The hydride anion in an extended transition metal oxide array: $\text{LaSrCoO}_3\text{H}_{0.7}$. *Science* **295**, 1882–1884 (2002).
30. Lu, N. et al. Electric-field control of tri-state phase transformation with a selective dual-ion switch. *Nature* **546**, 124–128 (2017).
31. Osada, M. et al. Nickelate superconductivity without rare-earth magnetism: $(\text{La},\text{Sr})\text{NiO}_2$. *Adv. Mater.* **33**, 2104083 (2021).
32. Williams, J. H. The molecular electric quadrupole moment and solid-state architecture. *Acc. Chem. Res.* **26**, 593–598 (1993).
33. Radaelli, P. G. et al. Formation of isomeric Ir^{3+} and Ir^{4+} octamers and spin dimerization in the spinel CuIr_2S_4 . *Nature* **416**, 155–158 (2002).

34. Khomskii, D. I. & Streitsov, S. V. Orbital effects in solids: basics, recent progress, and opportunities. *Chem. Rev.* **121**, 2992–3030 (2021).
35. Chowdhury, S. et al. Negative charge-transfer energy in $\text{SrCoO}_{2.5}$ thin films: an interplay between O-2p hole density, charge-transfer energy, charge disproportionation, and ferromagnetic ordering. *ACS Appl. Electron. Mater.* **2**, 3859–3870 (2020).
36. Potze, R. H., Sawatzky, G. A. & Abbate, M. Possibility for an intermediate-spin ground state in the charge-transfer material SrCoO_3 . *Phys. Rev. B* **51**, 11501–11506 (1995).
37. Cui, B. et al. Direct imaging of structural changes induced by ionic liquid gating leading to engineered three-dimensional meso-structures. *Nat. Commun.* **9**, 3055 (2018).
38. Hidaka, M., Inoue, K., Yamada, I. & Walker, P. J. X-ray diffraction study of the crystal structures of K_2CuF_4 and $\text{K}_2\text{Cu}_x\text{Zn}_{1-x}\text{F}_4$. *Physica B+C* **121**, 343–350 (1983).
39. Aguado, F., Rodríguez, F., Valiente, R., Señas, A. & Goncharenko, I. Three-dimensional magnetic ordering in the Rb_2CuCl_3 layer perovskite—structural correlations. *J. Phys. Condens. Matter* **16**, 1927–1938 (2004).
40. Cammarata, A. & Rondinelli, J. M. Ferroelectricity from coupled cooperative Jahn–Teller distortions and octahedral rotations in ordered Ruddlesden–Popper manganates. *Phys. Rev. B* **92**, 14102 (2015).

Publisher's note Springer Nature remains neutral with regard to jurisdictional claims in published maps and institutional affiliations.

© This is a U.S. Government work and not under copyright protection in the US; foreign copyright protection may apply 2023

Methods

Synthesis of CaCoO_{2.5} thin films

Brownmillerite CaCoO_{2.5} thin films were synthesized by pulsed laser deposition on perovskite SrTiO₃ (001) substrates. We used a CaCoO_{2.5} polycrystalline target and a krypton fluoride excimer laser (wavelength $\lambda = 248$ nm, pulse repetition rate of 3 Hz and laser fluence of 1 J cm⁻²). The distance between the target and the substrate was maintained at about 50 mm. The optimal conditions for high-quality CaCoO_{2.5} films were found to be a substrate temperature $T = 600$ °C under oxygen partial pressure $P_{O_2} = 50$ mtorr. To protect the cobaltate films from potential degradation during and after the reduction process, we capped the as-grown CaCoO_{2.5} with five-unit cells of SrTiO₃. The precursor CaCoO_{2.5} film was then reduced to CaCoO₂ by topotactic reduction. We loosely covered the CaCoO_{2.5} film with aluminium foil and sealed it with about 0.1 g CaH₂ powder in a vacuum glass tube. We annealed the sealed tube at 250 °C for 3 h in a tube furnace. The thermal ramping and cooling rates were 10 °C min⁻¹.

STEM measurements

STEM specimens were prepared using a Thermo Fisher Scientific Helios G4 UX focused ion beam. Cross-section samples were prepared and thinned to electron transparency using standard lift-out and thinning methods. Plan-view samples were prepared first using the standard lift-out method and then attached to a half grid at a 90° angle to the standard orientation and thinned. Total air exposure of the prepared STEM specimens was limited to less than 15 min to minimize possible degradation of the films.

HAADF and ABF-STEM data were acquired using a Thermo Fisher Scientific Spectra 300 X-CFEG operating at 120 kV or 300 kV with a convergence angle of 30 mrad. Inner and outer collection angles were approximately 60 mrad and 200 mrad, respectively, for HAADF and 15 mrad and 30 mrad, respectively, for ABF imaging. To obtain high-signal-to-noise ratio (SNR) images, many fast-acquisition images were acquired and subsequently aligned using a rigid registration process optimized for noisy images⁴¹. Owing to electron beam sensitivity of the sample, a probe current of less than 30 pA was used for all STEM data acquisitions. EELS measurements therefore required total acquisition times of about 5,000 s for each spectrum to achieve a sufficient SNR to distinguish differences in the EELS fine structure. The spectra presented are aligned and summed series of several acquisitions. To ensure stage stability sufficient for such long acquisitions, a Nion UltraSTEM operated at 100 kV and equipped with a high-stability stage, an Enfinium ER spectrometer and Quefina2 camera was used to acquire all EELS data. The effective energy resolution, measured by the full-width at half-maximum of the zero-loss peak, was about 0.34 eV. To ensure consistency, spectra from multiple regions of each sample were acquired. The individual spectra for each edge were first aligned with respect to each other and summed to produce high-SNR measurements for the as-grown and reduced films. Absolute energy alignments were then applied to the Co L_{3,2} and Ca L_{3,2} edges and the O K-edges based on the Ti L_{3,2} and O K-edges of the SrTiO₃ substrate, respectively, which serve as well studied and consistent references. White line ratios were calculated from the Co L_{3,2} edges using the Pearson method.

Synchrotron GIXRD

The synchrotron GIXRD experiments were performed at room temperature (293 K) using the Huber six-circle diffractometer at the 3A beamline of the Pohang Light Source-II in South Korea. The incident beam from an undulator source was monochromatized to 1.1078 Å. The incident beam angle was fixed to 0.2°. The synchrotron XRD data were collected in a 2θ range from 0° to 75° with a step interval of 0.01°.

Refinement of the oxygen positions

We developed an initial estimate for the oxygen positions based on ABF-STEM images and the available phonon distortion modes given

the observed symmetry. We identified these phonon modes using the software package ISODISTORT, part of the ISOTROPY suite, which selects atomic displacement modes available when transitioning from a parent symmetry to a lower-symmetry structure^{42,43}. We then used the application ISOVIZ to visualize these displacement modes and to manually identify the combination of modes that best matched the ABF-STEM contrast⁴². These initial oxygen positions (as well as the cation positions deduced from HAADF-STEM) were then used to further refine the GIXRD peaks by the Rietveld method. We used the least-squares method to minimize the function $M = \sum_i \{I_i^{\text{obs}} - I_i^{\text{calc}}\}^2$, where I_i^{obs} and I_i^{calc} are the observed and calculated integrated Bragg peak intensity of the i th (hkl) plane. We used seven independent (hkl) planes for the refinement. The calculated Bragg peak intensity for the (hkl) plane is given as $I_{hkl}^{\text{calc}} = K p_{hkl} L_\theta |F_{hkl}|^2$, where K , p_{hkl} , L_θ and F_{hkl} are the scaling factor, number of equivalent (hkl) planes, Lorentz polarization factor and structure form factor, respectively. We used the R factor, $R = \frac{\sum_i |I_i^{\text{obs}} - I_i^{\text{calc}}|}{\sum_i I_i^{\text{obs}}}$, to quantify the goodness of fit.

Sample characterization

The conventional XRD data were taken using a monochromatized Cu Kα₁ source ($\lambda = 1.5406$ Å). The resistivity was measured using aluminium-wire-bonded contacts in a Hall bar geometry.

TOF-SIMS

TOF-SIMS characterization was performed using TOF.SIMS.5 NSC instrument (ION.TOF). A primary Bi⁺ ion beam with an energy of 30 keV, d.c. current of 30 nA and a spot size of about 5 μm was used for extraction of the secondary ions of the analysed sample. A complimentary Cs⁺ sputtering beam with an energy of 500 eV and a current of 40 nA was used for depth profiling. A low-energy unfocused electron flood gun was used for charge compensation. Measurements were performed in non-interlaced mode, where each scan with Bi⁺ (100 μm × 100 μm, 4 s duration) was followed by a sputtering cycle with Cs⁺ (300 μm × 300 μm, 2 s duration). A TOF mass analyser operated in positive-ion mode was used to analyse secondary ions with a mass resolution $m/\Delta m = 2,000$ –5,000. The acquired chemical data provide one-dimensional depth profiles, characterizing the distribution of the elements of interest through the sample thickness. Depth calibration was performed using the known sample thickness in the assumption of homogeneous sputter rates.

DFT calculations

The initial structure was taken with all the atoms positioned at high-symmetry points of the simple tetragonal structure with a $2\sqrt{2}a_t \times 2\sqrt{2}a_t \times 2c_t$ supercell. Then structural relaxation was implemented with this initial structure using DFT + U calculations, where the Perdew–Burke–Ernzerhof⁴⁴ exchange-correlation functional was used and DFT + U was treated using the simplified (rotationally invariant) approach introduced by ref.⁴⁵. All DFT + U calculations were performed using the Vienna Ab initio Simulation Package (VASP)⁴⁶. The structural relaxation and self-consistent calculations were performed with $8 \times 8 \times 16$ Monkhorst–Pack momentum points, whereas the density of states calculations were performed with $20 \times 20 \times 40$ Monkhorst–Pack momentum points. It is noted that DFT + U calculations with various U values were explored, and 5 eV was chosen as the onset of opening a gap. The obtained relaxed structure shows the same structural symmetry breaking as found in the experimental structure but with smaller distortions. The magnitude and symmetry of the distortion are robust to variations in U values (Extended Data Fig. 5). To further investigate the stability of the distorted structure, we implemented generalized gradient approximation (GGA) + U , strongly constrained and appropriately normalized semilocal density functional (SCAN)⁴⁷, and SCAN + U calculations, on a series of structures with different distortions from zero up to the experimental distortion, as shown in Extended Data Fig. 6. We find that the DFT + U relaxed structure always shows

the lowest energy regardless of the calculation method used. Although none of the three methods predicts the amplitude of the experimental structure with the lowest energy, the symmetry-distorted structure (DFT + U relaxed structure) exhibits lower energy than the non-distorted one, showing the tendency of spontaneous symmetry breaking for the infinite-layer CaCoO_2 structure.

Cluster multiplet calculations

The calculations were performed by exact diagonalization of the CoO_2 11-orbital cluster involving 5 Co $3d$ orbitals and 6 O $2p$ orbitals forming 90° bond angles. The Hubbard–Kanamori interaction for O and Co orbitals captures multiplet energy levels parameterized by Slater–Condon integrals F . Hybridization is included through tight-binding hopping; charge transfer energy Δ and crystal field levels ε are chosen to give a high-spin Co $3d^7$ ground state (total spin $3/2$, 8-fold ground-state degeneracy) for the undistorted plaquette. A JT perturbation that lifts the ground-state degeneracy is applied by changing relative orbital energies for $3d_{xz}$ and $3d_{yz}$, which maintains the high-spin ground state, while reducing the degeneracy to 4. Increasing the hybridization (hopping) along the x bond directions reduces the degeneracy to 2 and creates a low-spin ground state characterized by $3d^8\text{L}$ with a ligand hole occupancy in the $2p_x$ orbital. Parameters are given in Extended Data Table 4.

Data availability

The data presented in the figures and other findings of this study are available from the corresponding authors upon reasonable request.

41. Savitzky, B. H. et al. Image registration of low signal-to-noise cryo-STEM data. *Ultramicroscopy* **191**, 56–65 (2018).
42. Campbell, B. J., Stokes, H. T., Tanner, D. E. & Hatch, D. M. ISODISPLACE: a web-based tool for exploring structural distortions. *J. Appl. Crystallogr.* **39**, 607–614 (2006).
43. Stokes, H. T., Hatch, D. M. & Wells, J. D. Group-theoretical methods for obtaining distortions in crystals: applications to vibrational modes and phase transitions. *Phys. Rev. B* **43**, 11010–11018 (1991).
44. Perdew, J. P., Burke, K. & Ernzerhof, M. Generalized gradient approximation made simple. *Phys. Rev. Lett.* **77**, 3865–3868 (1996).
45. Dudarev, S. L., Botton, G. A., Savrasov, S. Y., Humphreys, C. J. & Sutton, A. P. Electron-energy-loss spectra and the structural stability of nickel oxide: an LSDA+ U study. *Phys. Rev. B* **57**, 1505–1509 (1998).
46. Kresse, G. & Hafner, J. Ab initio molecular dynamics for liquid metals. *Phys. Rev. B* **47**, 558–561 (1993).
47. Sun, J., Ruzzinszky, A. & Perdew, J. P. Strongly constrained and appropriately normed semilocal density functional. *Phys. Rev. Lett.* **115**, 036402 (2015).
48. Tassel, C. et al. CaFeO_2 : a new type of layered structure with iron in a distorted square planar coordination. *J. Am. Chem. Soc.* **131**, 221–229 (2009).
49. Goodge, B. H. et al. Doping evolution of the Mott–Hubbard landscape in infinite-layer nickelates. *Proc. Natl. Acad. Sci. USA* **118**, e2007683118 (2021).
50. Momma, K. & Izumi, F. VESTA: a three-dimensional visualization system for electronic and structural analysis. *J. Appl. Crystallogr.* **41**, 653–658 (2008).

Acknowledgements We thank W.-S. Lee for discussions. The work at SLAC and Stanford was supported by the US Department of Energy (DOE), Office of Basic Energy Sciences, Division of Materials Sciences and Engineering (contract number DE-AC02-76SF00515) and the Gordon and Betty Moore Foundation’s Emergent Phenomena in Quantum Systems Initiative (grant number GBMF9072, synthesis equipment and initial development). Electron microscopy at Cornell was support by the Department of Defense Air Force Office of Scientific Research (number FA 9550-16-1-0305) and the Packard Foundation, and made use of the Cornell Center for Materials Research Shared Facilities which are supported through the NSF MRSEC programme (DMR-1719875), with the Thermo Fisher Helios G4 UX focused ion beam also supported by NSF (DMR-1539918). The Thermo Fisher Spectra 300 X-CFEG was acquired with support from PARADIM, an NSF MIP (DMR-2039380), and Cornell University. M.A.S. acknowledges additional support from the NSF GRFP under award number DGE-1650441. The 3A beamline at PLS-II is supported in part by MSIT. B.-G.C. is currently affiliated to Korea Research Institute of Standards and Science (KRISS). D.J. acknowledges funding by the Alexander-von-Humboldt foundation via a Feodor Lynen postdoctoral fellowship. Raman spectroscopy measurement was performed at the Stanford Nano Shared Facilities (SNSF), supported by the National Science Foundation under award ECCS-2026822. TOF-SIMS characterization was conducted at the Center for Nanophase Materials Sciences, which is a DOE Office of Science User Facility, and using instrumentation within ORNL’s Materials Characterization Core provided by UT-Battelle, LLC under contract number DE-AC05-00OR22725. The computational work for this project was performed on the Sherlock cluster in the Stanford Research Computing Center.

Author contributions W.J.K. and H.Y.H. conceived and designed the experiments. M.A.S., B.H.G. and L.F.K. performed the STEM and EELS measurements and analysis. C.J. performed the DFT calculations. C.J., B.M. and T.P.D. performed the cluster calculations. D.J. performed Raman spectroscopy measurements. W.J.K. grew the samples, which were characterized by W.J.K., K.L., D.J. and M.O. W.J.K. and B.-G.C. performed and analysed the synchrotron GIXRD measurements. A.V.I. performed TOF-SIMS measurements. W.J.K., T.P.D. and H.Y.H. wrote the manuscript, with input from all authors.

Competing interests The authors declare no competing interests.

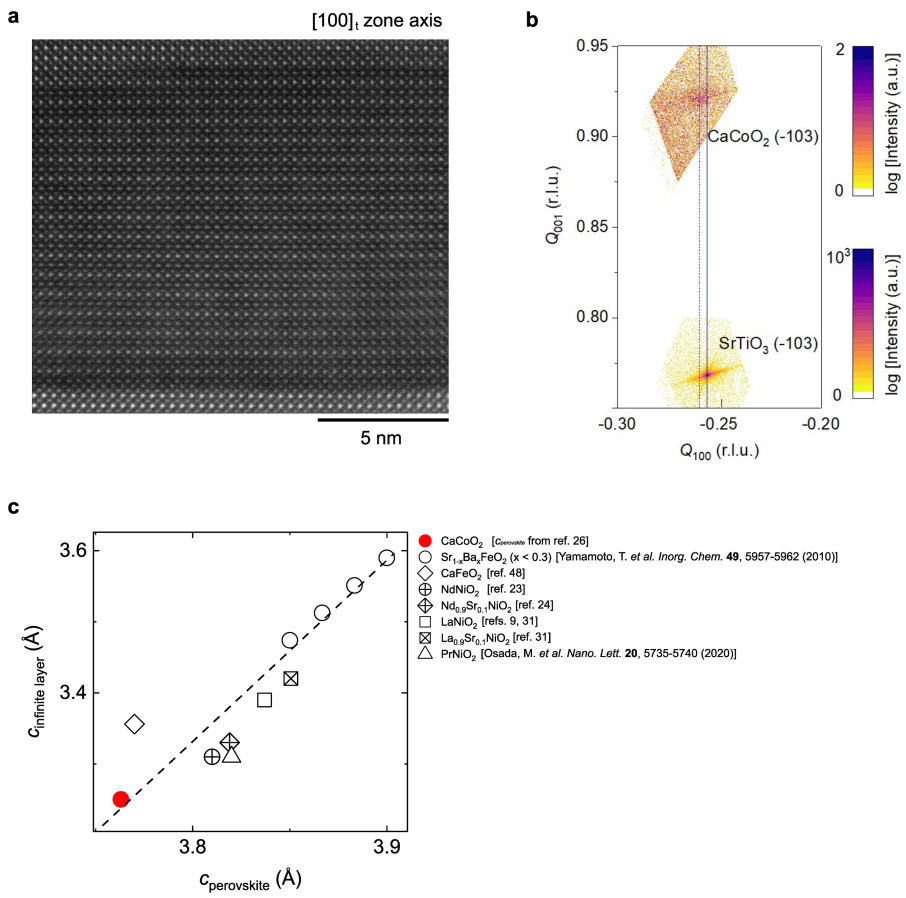
Additional information

Supplementary information The online version contains supplementary material available at <https://doi.org/10.1038/s41586-022-05681-2>.

Correspondence and requests for materials should be addressed to Woo Jin Kim or Harold Y. Hwang.

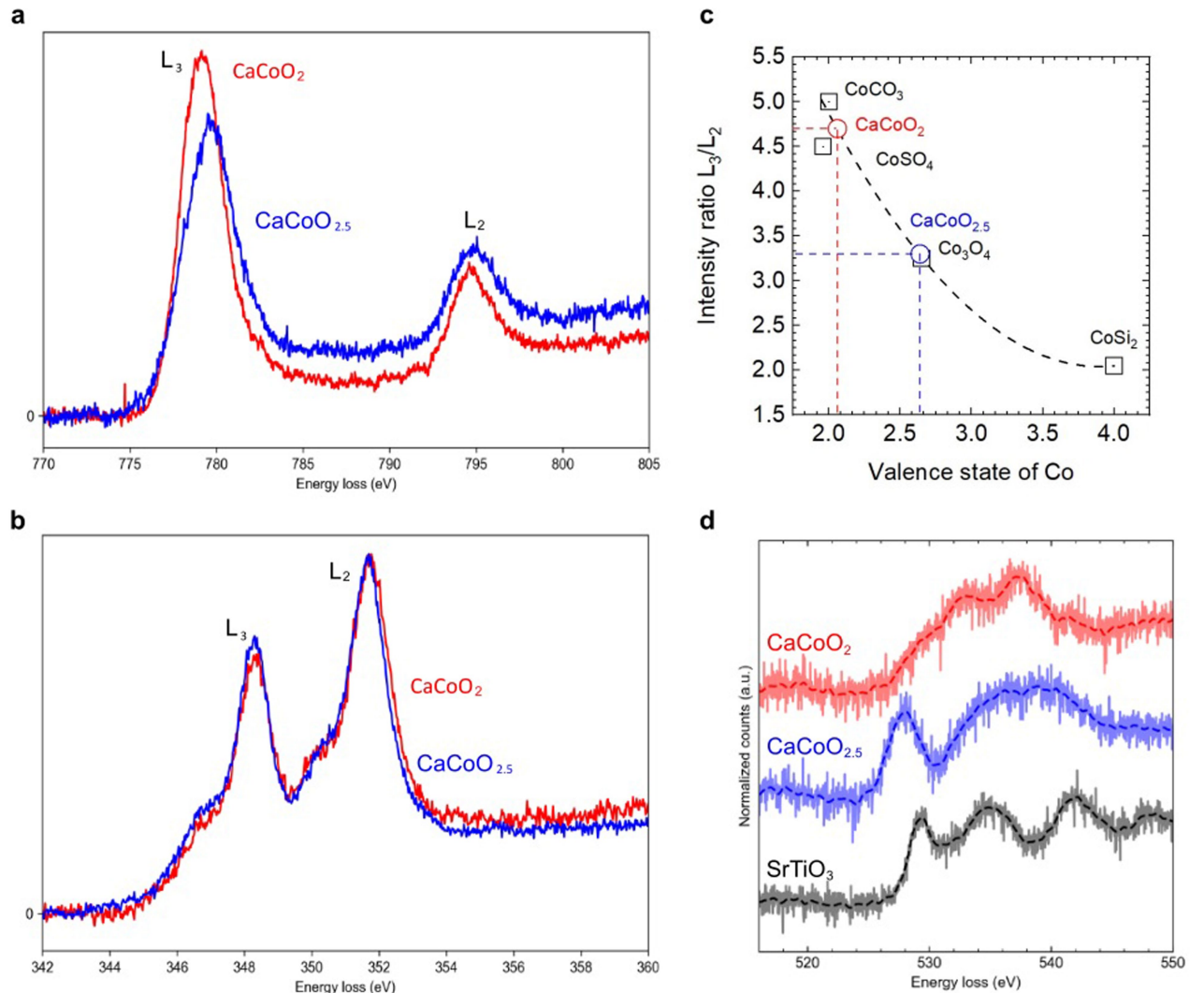
Peer review information *Nature* thanks Eric Hoglund and the other, anonymous, reviewer(s) for their contribution to the peer review of this work. Peer reviewer reports are available.

Reprints and permissions information is available at <http://www.nature.com/reprints>.



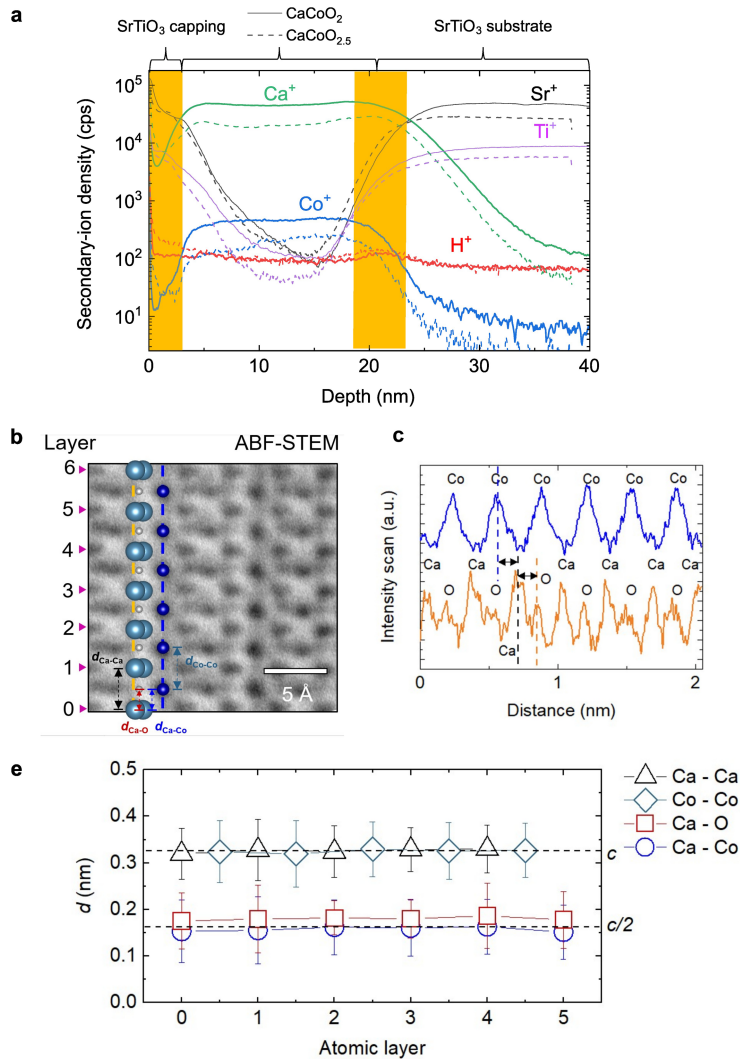
Extended Data Fig. 1 | Structural characterizations for CaCoO_{2.5} and CaCoO₂. **a**, Atomic-resolution HAADF-STEM image along the [100]_t zone-axis projection of CaCoO_{2.5} showing alternate stacking of tetrahedral and octahedral layers. **b**, X-ray diffraction reciprocal space map of CaCoO₂ around the (-103) SrTiO₃ diffraction peak, indicating that the film is relaxed from the substrate. **c**, Empirical relationship between perovskite and infinite-layer

lattice parameters. c -axis lattice parameters for various transition metal oxide compounds are plotted for the perovskite phase and the infinite-layer phase after topotactic reduction. The dashed line is a linear fit for all the data points in the plot. Note that the CaFeO₂ has relatively large $c_{\text{infinite layer}}/c_{\text{perovskite}}$ associate with out-of-plane displacement of both FeO₄ and Ca layers⁴⁸.



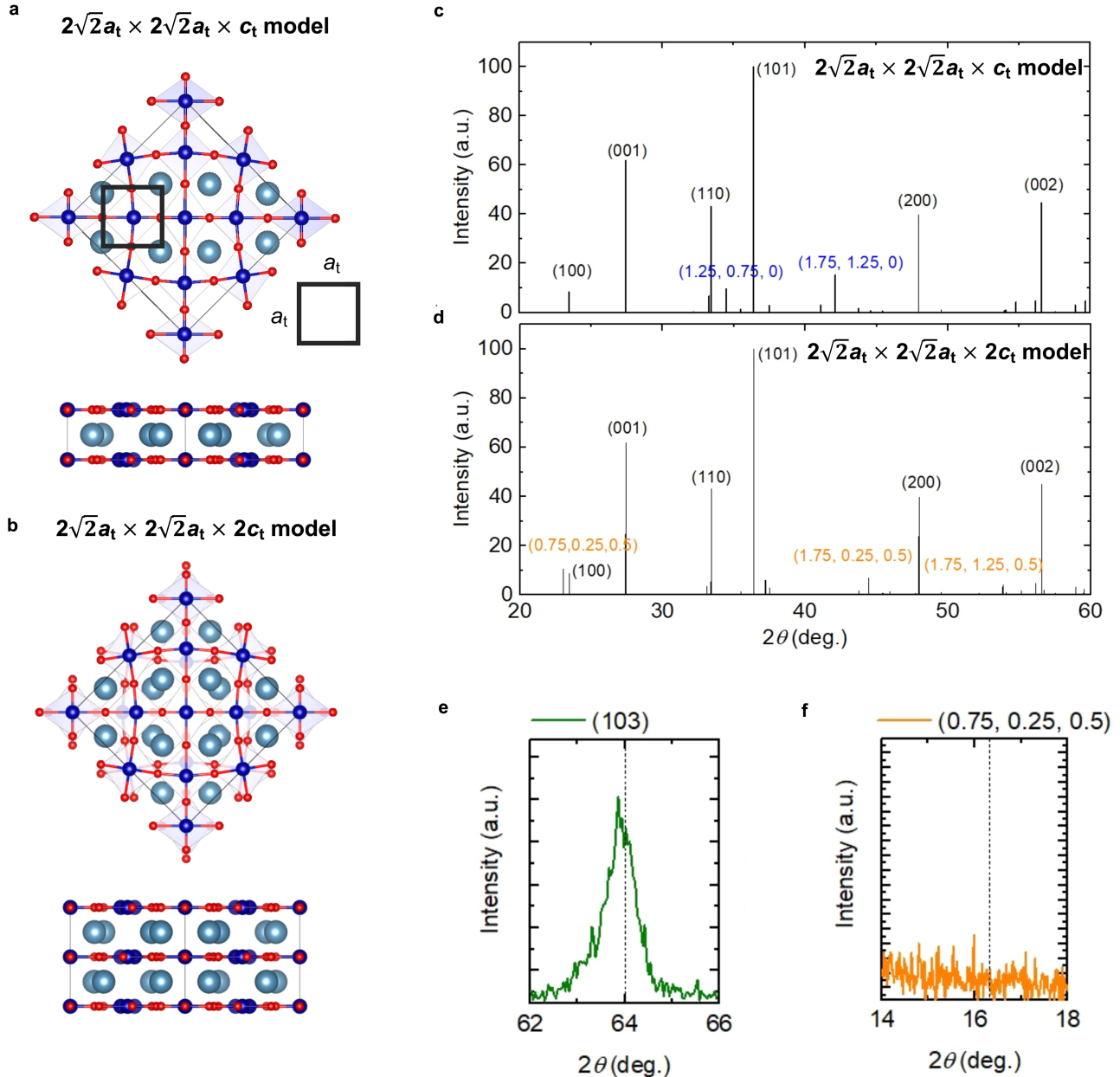
Extended Data Fig. 2 | EELS measurements of CaCoO_2 . **a**, $\text{Co}-L_{3,2}$ edge; the blue (red) solid line indicates EEL spectra for $\text{CaCoO}_{2.5}$ (CaCoO_2). **b**, $\text{Ca}-L_{3,2}$ edge EELS shows that there are no substantial changes in the spectra before ($\text{CaCoO}_{2.5}$, blue) and after reduction (CaCoO_2 , red). **c**, A plot of the intensity ratio $I(L_3)/I(L_2)$ of the $\text{Co}-L_{3,2}$ edge for different Co compounds with different oxidation states. Note that the dashed line indicates a polynomial fit curve for four different compounds from ref.²⁷ (CoCO_3 , CoSO_4 , Co_3O_4 , and CoSi_4). $I(L_3)/I(L_2)$ of the $\text{CaCoO}_{2.5}$ and CaCoO_2 films are depicted with blue and red circles, respectively. **d**, O K-edges EELS data. Spatially averaged O K-edge spectra of CaCoO_2 ($\text{CaCoO}_{2.5}$) in red (blue). The partially transparent, solid lines indicate the raw, background-subtracted data, and the dashed lines indicate

the Gaussian filtered spectra. Upon reduction of the $\text{CaCoO}_{2.5}$ films to CaCoO_2 , we observe a suppression of the distinct pre-peak at ~529 eV in the region of the O K-edge associated with hybridization between O $2p$ and transition metal d orbitals consistent with a nominal electronic transition from $3d^6$ to $3d^7$. This is similar to the pre-peak suppression observed upon reduction from perovskite to infinite-layer phase in the related nickelates⁴⁹. We further see the emergence of a shoulder in the CaCoO_2 spectrum at ~530 eV, which is similar to a feature attributed to ligand hole states in doped infinite-layer nickelates⁴⁹. This feature is also consistent with published spectra acquired from SrCoO_{3-6} , which has negative charge transferred state³⁷. An O K-edge spectrum of the SrTiO_3 substrate is included in black for comparison.



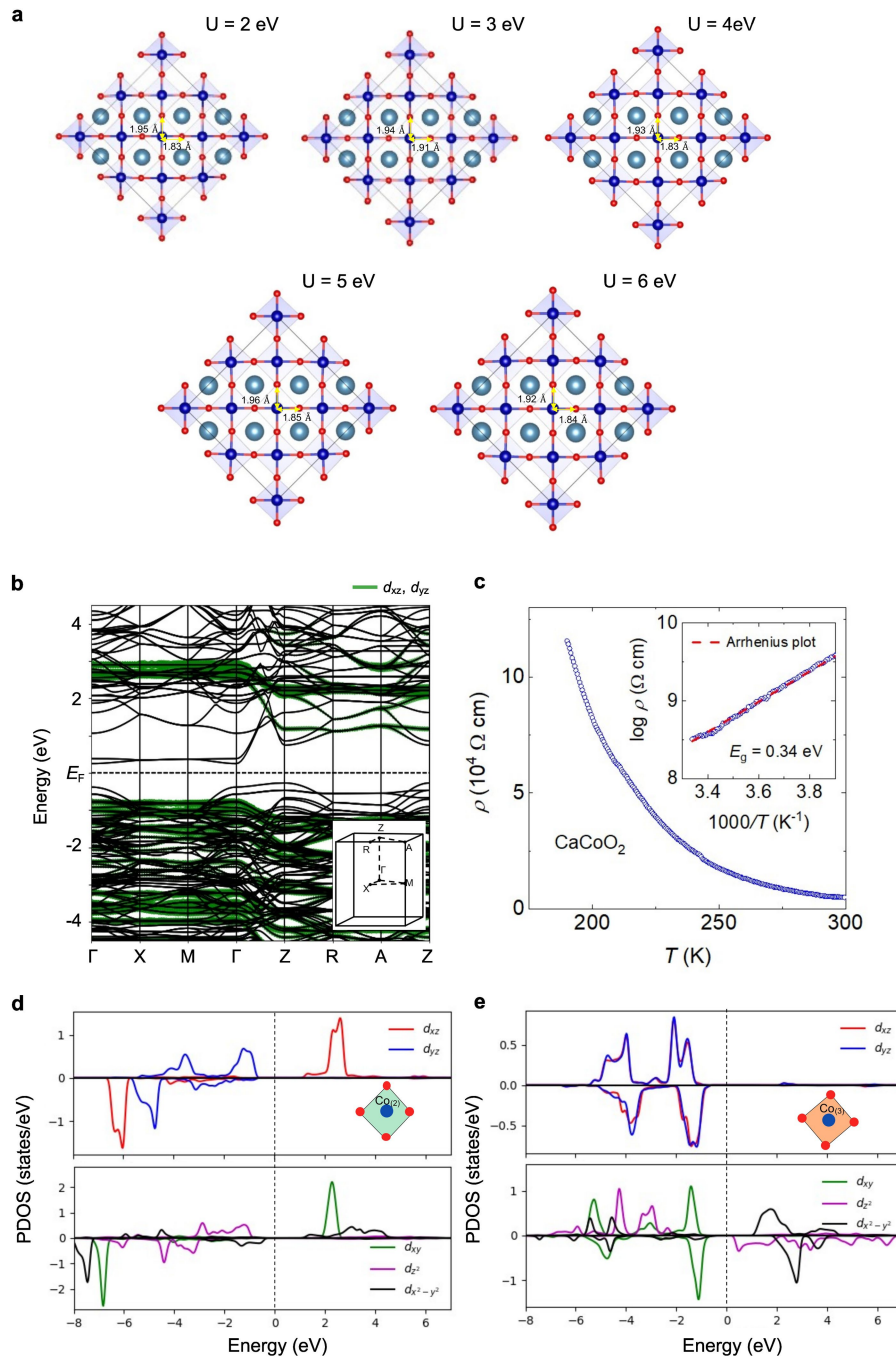
Extended Data Fig. 3 | Time-of-flight secondary-ion mass spectrometry (TOF-SIMS) and ABF-STEM measurements of CaCoO₂. **a**, Depth profiles of H⁺ and other ions from both CaCoO_{2.5} and CaCoO₂ thin film on SrTiO₃ substrate (with ~2 nm SrTiO₃ capping layer) were measured with secondary-ion mass spectrometry. The Co ion signals from both CaCoO_{2.5} and CaCoO₂ thin films were employed as a marker for the interface position. TOF-SIMS measurements show that the H⁺ concentration for CaCoO₂ is similar to the background level of the as-synthesized CaCoO_{2.5} thin film. **b**, ABF-STEM image along the [100] zone-axis projection with overlaid Co, Ca, and O atoms. **c**, Intensity line profiles

for the blue and the orange dashed lines in **b**. The intensities of the line profiles are from inverted image **b**. The blue (orange) solid line indicates the line profile for the Co column (Ca and O column). The peak positions are the relative distances noted at the bottom of the image **b**. **d**, Atomic distances between Ca and Ca (black triangles), Co and Co (green diamonds), Ca and O (red squares), and Ca and Co (blue circles) layers are plotted. Note that the atomic layer numbers in **d** correspond to those in **b**. Error bars are taken as the full-width at half-maximum of the intensity peaks in **c**.



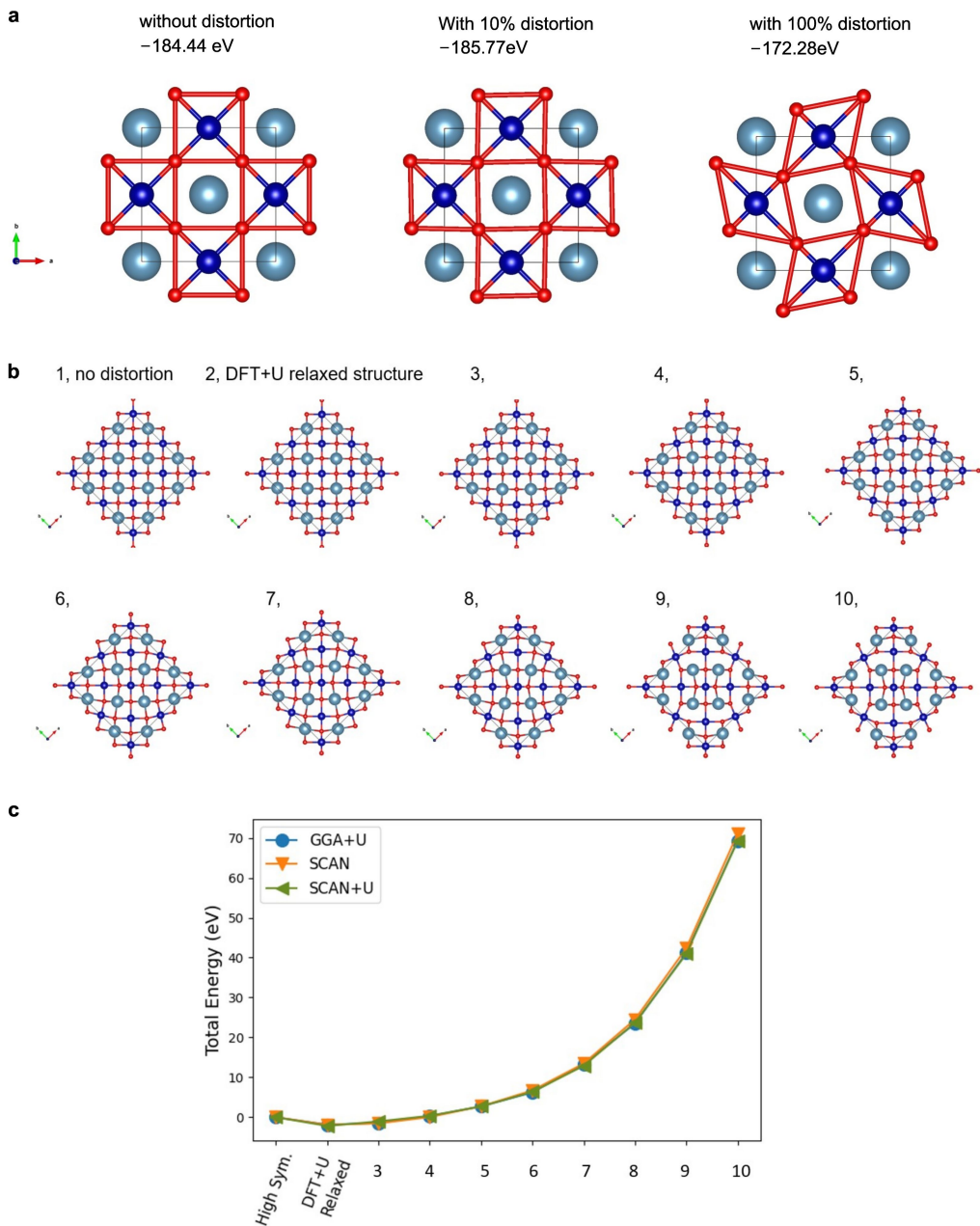
Extended Data Fig. 4 | Powder XRD simulation and *c*-lattice parameter determination. Lattice structure models for **a**, $2\sqrt{2}a_t \times 2\sqrt{2}a_t \times c_t$, and **b**, $2\sqrt{2}a_t \times 2\sqrt{2}a_t \times 2c_t$. The second structure model is lattice doubled from the first model by stacking a half-unit-cell shifted layer along the in-plane direction. Powder XRD simulation results for both **c**, $2\sqrt{2}a_t \times 2\sqrt{2}a_t \times c_t$ and **d**, $2\sqrt{2}a_t \times 2\sqrt{2}a_t \times 2c_t$ models. Note that the XRD simulation for the $2\sqrt{2}a_t \times 2\sqrt{2}a_t \times 2c_t$ model has a

distinct half-order peak along the *c*-lattice direction. We first found **e**, the $\text{CaCoO}_2(103)$, XRD peak as a reference peak. Based on this reference peak position, we perform θ - 2θ scans along the expected $\text{CaCoO}_2(0.75, 0.25, 0.5)$ position. **f**, No XRD peak was observed at the expected $\text{CaCoO}_2(0.75, 0.25, 0.5)$ peak position, indicating that CaCoO_2 does not have a *c*-axis doubling of the simple tetragonal unit cell.



Extended Data Fig. 5 | DFT calculations for CaCoO₂. **a**, Plan-view of the relaxed crystal structure for CaCoO₂ from DFT + U calculations with U = 2 eV, U = 3 eV, U = 4 eV, U = 5 eV, and U = 6 eV. **b**, Calculated band dispersion of CaCoO₂ (DFT + U for U = 5 eV). Green highlights d_{xz} (and d_{yz}) projections. The inset shows high-symmetry points in the tetragonal Brillouin zone. **c**, Resistivity versus

temperature of CaCoO₂ thin film. The inset shows that the resistivity is well fitted with an Arrhenius plot with an estimated (transport) gap of $0.337 \pm 0.001 \text{ eV}$. The spin-dependent partial density of states (PDOS) of **d**, Co₍₂₎ and **e**, Co₍₃₎ d orbitals from DFT + U (U = 5 eV). The spin-dependent PDOS of Co₍₂₎ shows the degeneracy lifting of the $d_{xz/yz}$ -orbitals.



Extended Data Fig. 6 | Total energy calculation for CaCoO_2 with $\sqrt{2} \times \sqrt{2} \times 1$ and $2\sqrt{2} \times 2\sqrt{2} \times 1$ supercell. **a**, DFT+U ($U=5$ eV) calculations for the total energy under purely Q_2 -JT-distortions in the $\sqrt{2} \times \sqrt{2} \times 1$ supercell. **b**, $2\sqrt{2} \times 2\sqrt{2} \times 1$ supercell with different distortion amplitudes. Approaching #10, the structure

is approached the experimentally refined structure. **c**, Normalized total energy for the structures depicted in **b**. Three different first-principle calculations are used for **c** (Methods).

Article

Extended Data Table 1 | Atomic coordinates for the initial (before GIXRD refinement) and refined structure of CaCoO₂

Atom	P42 ₁ 2 symmetry group						
	x		y		z		Occupation
	Initial	Refined	Initial	Refined	Initial	Refined	
Co ₍₁₎	0	0	0	0	0	0	1
Co ₍₂₎	0.200	0.205 ± 0.011	0.200	0.205 ± 0.011	0	0	1
Co ₍₃₎	0.500	0.500	0	0	0	0	1
Ca	0.460	0.459 ± 0.012	0.250	0.255 ± 0.011	0.500	0.500	1
O ₍₁₎	0.349	0.349 ± 0.010	0.099	0.099 + 0.010	0	0	1
O ₍₂₎	0.349	0.363 ± 0.012	0.349	0.363 ± 0.012	0	0	1
O ₍₃₎	0.099	0.078 ± 0.011	0.099	0.078 ± 0.011	0	0	1

Initial atomic coordinates were taken from the values from the STEM measurements.

Extended Data Table 2 | Simulated and experimental CaCoO₂ (HKO) GI-XRD peak positions and intensities

Photon energy 11.2 keV (0.11078 nm)								
<i>h</i>	<i>k</i>	<i>l</i>	$\phi_{sim.}$ (°)	$\phi_{exp.}$ (°)	$2\theta_{sim.}$ (°)	$2\theta_{exp.}$ (°)	Intensity _{sim.} (a.u.)	Intensity _{exp.} (a.u.)
1.25	0.75	0	30.96	30.83 ± 0.002	24.47	24.10 ± 0.001	9.92	1406 ± 13
0.5	1.5	0	18.43	18.31 ± 0.002	26.58	26.24 ± 0.002	3.03	574 ± 10
1.75	0.25	0	8.13	7.72 ± 0.002	29.79	29.33 ± 0.002	15.10	2162 ± 20
2.25	1.75	0	37.88	37.74 ± 0.003	48.96	48.24 ± 0.004	5.04	366 ± 8
2.75	0.75	0	15.26	15.64 ± 0.032	48.96	48.14 ± 0.027	0.90	160 ± 29
2.5	1.5	0	30.96	31.02 ± 0.003	50.16	49.43 ± 0.003	3.48	704 ± 10
2.75	1.25	0	24.44	$24.53 + 0.035$	52.10	$51.10 + 0.034$	0.36	$46 + 7$

VESTA software⁵⁰ was used for the simulated GI-XRD peak positions and intensities.

Article

Extended Data Table 3 | Structure symmetry and atomic coordinates for the refined structure of CaCoO₂

Data collection	CaCoO ₂ (GIXRD refinement)				
Space group	<i>P</i> 42 ₁ 2 (No. 90)				
Cell dimensions	<i>a</i> , <i>b</i> , <i>c</i> (Å)				
<i>a</i> , <i>b</i> , <i>g</i> (°)	<i>a</i> = <i>b</i> = 10.78 Å, <i>c</i> = 3.27 Å α = β = γ = 90°				
Atomic coordination	Atom	<i>x</i>	<i>y</i>	<i>z</i>	<i>Occupation</i>
	Co ₍₁₎	0	0	0	1
	Co ₍₂₎	0.205 ± 0.011	0.205 ± 0.011	0	1
	Co ₍₃₎	0.500	0	0	1
	Ca	0.459 ± 0.012	0.255 ± 0.011	0.500	1
	O ₍₁₎	0.349 ± 0.010	0.099 ± 0.010	0	1
	O ₍₂₎	0.363 ± 0.012	0.363 ± 0.012	0	1
	O ₍₃₎	0.078 ± 0.011	0.078 ± 0.011	0	1

Extended Data Table 4 | Parameters used for multiplet calculations (in eV)

F_0	6
F_2	0.12857
F_4	0.025
Coulomb U_{dd}	7.4
Hund's J	0.886
Average Coulomb \bar{U}	5.45
$d_{x^2-y^2}$	0
d_{z^2}	2.4
d_{xy}	0.2
$d_{xz/yz}$	1.2
Δ	$3\bar{U}$
t_{pd}	1
t_{pdz}	$t_{pd}/4$
$t_{pdxy} = t_{pdxz} = t_{pdyz}$	0.225
$t_{pp\sigma}$	0.25
Coulomb U_{pp}	1

These parameters were used to generate the ground-state ($3d^7$) configuration for the cluster. The high-spin Jahn–Teller split ground state was obtained by lifting the degeneracy of the $d_{xz/yz}$ site energies, while the low-spin ground state was obtained by increasing all hybridizations along the x-direction of the cluster.